# High Fidelity Hall Effect Thruster Plume Simulations with Facility Carbon Sputterant Tracking

#### IEPC-2025-510

Presented at the 39th International Electric Propulsion Conference, Imperial College London, London,
United Kingdom
14-19 September 2025

Matthew J. Stasiukevicius\* and Iain D. Boyd<sup>†</sup>
University of Colorado Boulder, Boulder, CO, 80305, USA

Facility effects induced by vacuum chambers in ground-based electric propulsion testing complicate the extrapolation from ground test results to space performance. The sputtering of facility surfaces by energetic particles and the re-deposition of that material onto other facility or thruster surfaces is a particularly complicated facility effect that materializes in different ways. This work implements a reduced order sputtering model that calculates surface sputter yields, and sputtered particle trajectories into a high fidelity three dimensional Hall-effect thruster plume code. The implemented sputter model is verified within the plume code to produce expected sputter yields and sputter particle trajectories. The newly combined simulation tool is then applied to model a Hall-effect thruster plume sputtering experiment conducted in Vacuum Test Facility 2 at the Georgia Institute of Technology. Direct comparisons of the model are made with measurements of carbon sputtered onto collection arrays from a material test sample. Additional simulations predict facility-wide carbon sputtering. A variance-based sensitivity analysis is performed to assess the importance of plume model accuracy for sputtering simulation, and to inform which plasma diagnostics are most useful for understanding comparisons of experimental and simulation sputtering results.

## Nomenclature

 $\mathbf{E}$  = Electric field  $\phi$  = Electric potential

 $\mathbf{F}$  = Force

q = Particle Charge

 $N_{pairs}$  = Total particle pairs to be assessed for collision

 $N_P$  = Number of macroparticles

n = Number density

 $\sigma$  = Collision cross section

g = Relative velocity

 $\Delta t$  = Timestep

 $\epsilon_{coll}$  = Collision energy

 $\mathbf{v}$  = Velocity

e = Elementary charge

p = Pressure

<sup>&</sup>lt;sup>†</sup>H. T. Sears Memorial Professor, Ann and H.J. Smead Department of Aerospace Engineering Sciences.



 $<sup>^*</sup>$ PhD pre-candidate, Ann and H.J. Smead Department of Aerospace Engineering Sciences, matthew.stasiukevicius@colorado.edu.

 $\nu$  = Collision frequency

m = Mass

T = Temperature

 $k_B$  = Boltzmann constant

Y = Sputter yield

E = Energy  $\theta$  = Polar angle M = Molar mass Z = Atomic number

### I. Introduction

Electric propulsion (EP) thrusters are a flight proven technology with widespread use on satellites due to their high specific impulse, longevity, and reliability.<sup>1</sup> These characteristics of EP devices in general, and the high thrust-to-power ratio and relative simplicity of Hall-effect thrusters<sup>2</sup> (HETs), in particular, make HETs a desirable choice for long duration and deep space missions.<sup>3</sup> Such missions inherently require additional testing and qualification. EP devices are typically developed and tested in ground-based vacuum facilities that imperfectly recreate the space environment. These imperfections, or facility effects, include an elevated background pressure of neutral gas particles, deposition of sputtered facility surface materials onto thruster surfaces, and altered electrical pathways due to the presence of conducting facility walls. In particular, the deposition of sputtered material on thruster surfaces can negatively affect thruster performance.<sup>4</sup> Furthermore, this facility backsputter alters the performance and lifetime tests required for long duration space flight.<sup>5</sup> Under spaceflight conditions, trajectories of sputterants differ greatly from those in ground tests because of different sputter sources and altered plume characteristics such as background pressure and divergence angle. Moreover, space conditions include more surfaces that are concerned with sputtering and contamination including but not limited to: solar arrays, delicate sensors or experiments as well as thruster surfaces.<sup>6</sup>

Previous work has been done to characterize sputtering in EP test facilities. Some examples of previous work consists of comparisons of a theoretical sputter deposition model to experimental measurements in multiple facilities, development of novel experimental measurements combined with particle simulations, and investigations of how sputter and deposition rates vary in different regions of the plume. These works emphasize that accurate modeling of sputtering in ground chambers is an essential supplement to experimental tests for extrapolating results beyond the experiment and developing mitigation strategies.

With the aid of high-powered EP experiments in vacuum chambers, plume models that account for facility effects can help bridge the gap between ground and space conditions. In this study, a hybrid kinetic-continuum model is used to simulate the plume of the magnetically shielded H9 Hall Effect Thruster operating on krypton in Vacuum Test Facility 2 (VTF-2) at the Georgia Institute of Technology. Comparisons to data measured using plasma diagnostics and a sputtering experiment in VTF-2 are used to evaluate plume model and sputtering model accuracy. Simulations are then run to predict facility-wide surface sputtering and deposition rates. Additionally, a variance based sensitivity analysis of sputtered particle deposition rate to several simulation parameters is performed. The paper ends with a discussion of conclusions and future work.

## II. Experimental Overview

The Facility Interpolation Test 1 (FIT1) was a comprehensive experimental test campaign that was a collaboration of several universities as a part of the NASA-funded Joint Advanced Propulsion Institute (JANUS). Experiments of the FIT1 were all conducted in VTF-2 at Georgia Institute of Technology. VTF-2 is a cylindrical vacuum chamber 9.2 meters in length and 4.6 meters in diameter. VTF-2 employs ten liquid nitrogen-cooled PHPK TM1200i cryopumps which can keep operating pressure below  $6 \times 10^{-6}$  Torr-Kr.<sup>9</sup>

One part of the FIT1 campaign was an experiment to track isolated sputtered carbon in the far field plume from a designated sputtering target to collection arrays. A detailed overview of the experiment is

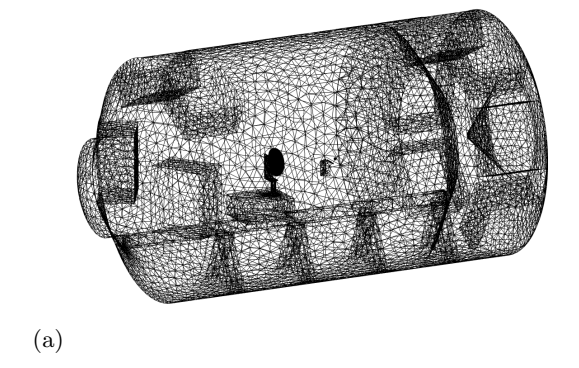


provided in Ref. 10. Carbon-13, an isotope with about one percent natural abundance, was used as the sputter target to measure deposition rate on the collection arrays specifically from the target. The carbon-13 deposition rate on the collection arrays was measured using a combination of the following techniques outlined in Ref. 10: optical surface profilometry, X-ray photoelectron spectroscopy, X-ray reflectometry, and time-of-flight secondary ion mass spectrometry. The computational mesh used to simulate VTF-2, and a sketch of the sputter experimental set-up are provided in Fig. 1.

The experiment used the H9 HET operating on krypton gas. The H9 is a magnetically shielded HET with a center mounted cathode; more information on the H9 can be found in Ref. 11. An overview of the operating conditions during the sputtering experiment is shown in Table 1.

Table 1: H9 operating conditions in VTF-2.

Propellant	Krypton
Discharge Voltage	600 V
Discharge Current	15 A
Flow Rate	$201.16~{\rm sccm}$
Background Pressure	$5.6~\mu\mathrm{Torr}$



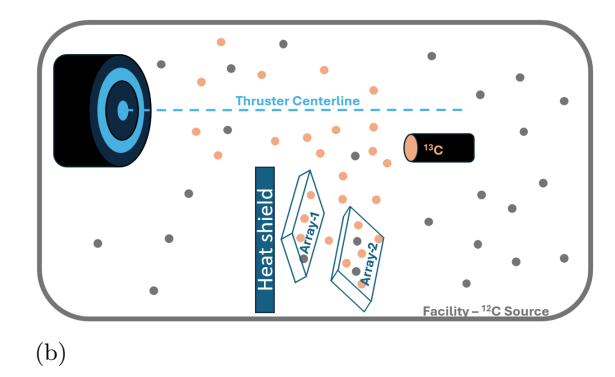


Figure 1: (a) Three dimensional computational mesh of VTF-2 used in MPIC. (b) Sketch outlining set-up of sputtering experiment performed in VTF-2.

## III. Methods

The hybrid particle-fluid simulation code MPIC<sup>12</sup> is used to simulate the plasma plume in the vacuum chamber. Near-field plume properties generated by the 2D axisymmetric multi-fluid Hall thruster code, Hall2De, <sup>13</sup> are used as input conditions for MPIC. Hall2De was originally developed at the Jet Propulsion Laboratory, but a version maintained by the University of Michigan is used in this work. A detailed description of Hall2De is available in the literature. 13,14 Hall2De thruster simulations are coupled to MPIC plume simulations using a weak coupling scheme developed in Ref. 15. Following this coupling scheme, species number densities, velocities, and temperatures are coupled from Hall2De to MPIC through fifty-two spatially varying inlets; the computational mesh of these inlets is shown in Fig. 2. In this version of Hall2De, each ion species, Kr<sup>+</sup>, Kr<sup>++</sup> and Kr<sup>+++</sup>, has two separately tracked populations, one for ions born above 240 V and one for ions born below 240 V. These separate ion populations are input to MPIC as separate populations with unique number densities, velocities, and temperatures at each inlet. Plots of number density, velocity, and temperature profiles across the thruster-plume interface for Kr and Kr<sup>+</sup> are provided in Figs. 3-5, and plots of the Kr<sup>+++</sup> and Kr<sup>+++</sup> current fraction profiles across the thruster-plume interface are shown in Fig. 6. Ion number density plots are total number density of both populations of ions, and velocity and temperature plots are averaged between the two populations weighted by population number density. To simulate surface material sputtering, a reduced order carbon sputter model is implemented into MPIC that is based on material multi-scale simulations. <sup>16</sup> The model informs sputter yields, sputtered particle angles and energies, and re-deposition.



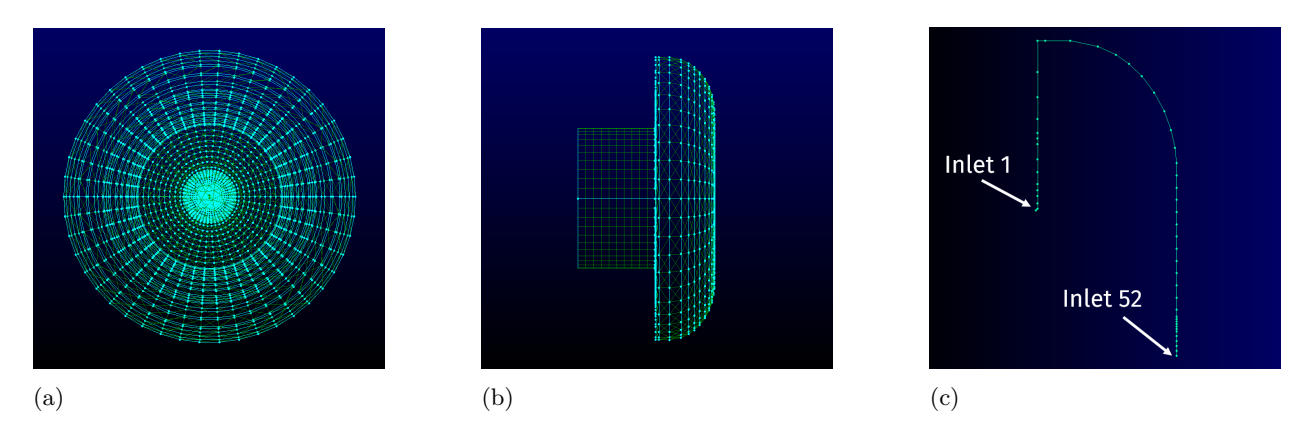


Figure 2: (a) Front and (b) and side views of the interface between Hall2De and MPIC. The cross-sectional view (c) shows the magnetic field line interface with labeled inlet numbers used to define spatially varying boundary conditions.

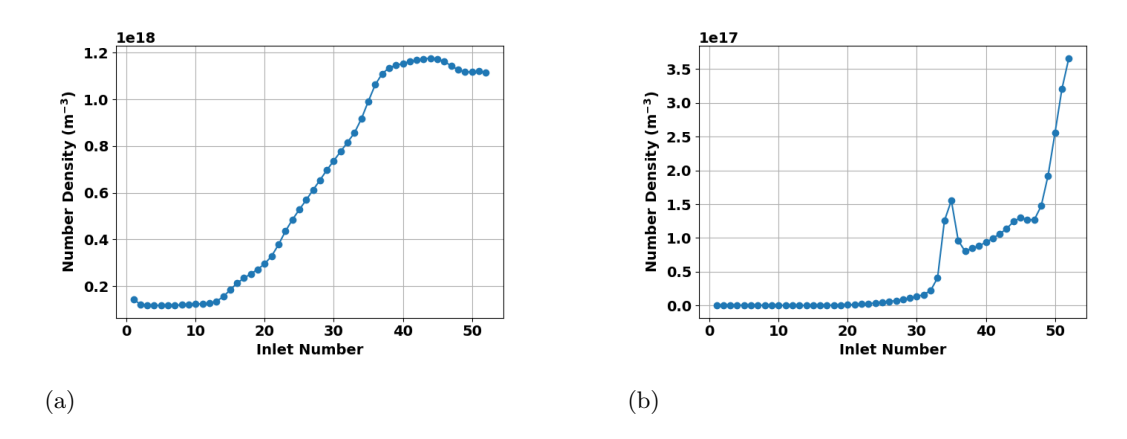


Figure 3: Profiles of (a) Kr and (b) Kr<sup>+</sup> number densities across the thruster-plume interface.

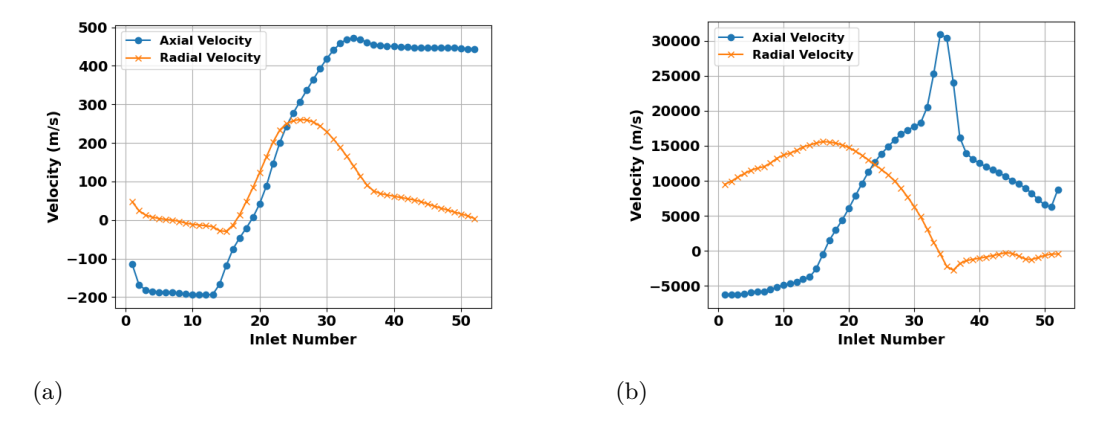


Figure 4: Profiles of (a) Kr and (b) Kr<sup>+</sup> velocities across the thruster-plume interface.



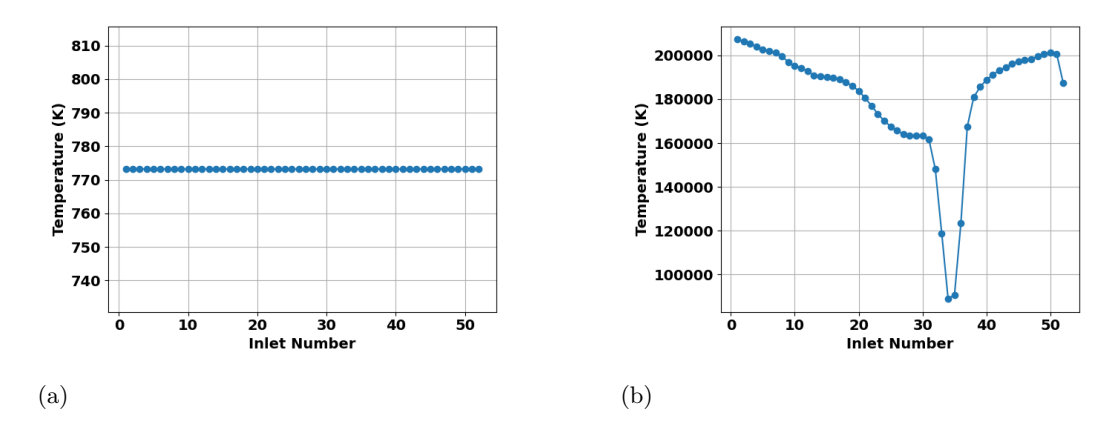


Figure 5: Profiles of (a) Kr and (b) Kr<sup>+</sup> temperatures across the thruster-plume interface.

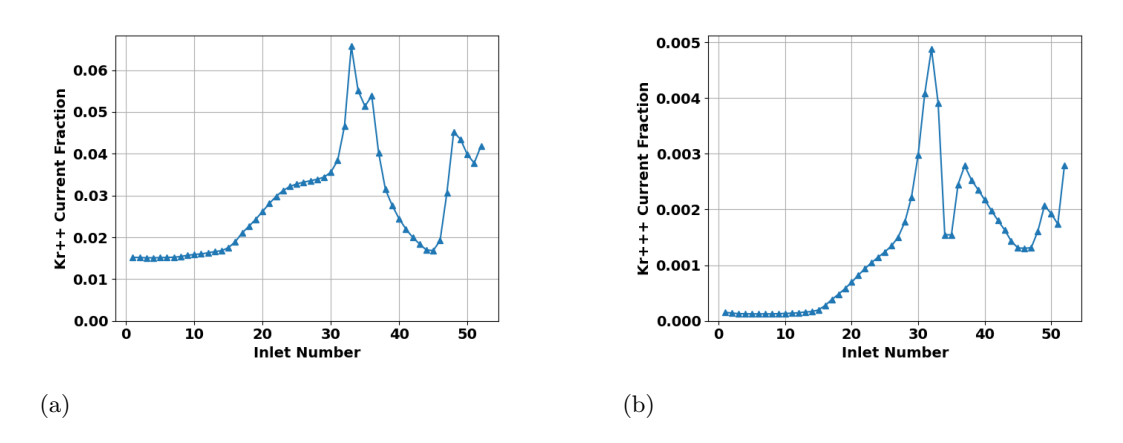


Figure 6: Profiles of (a) Kr<sup>++</sup> and (b) Kr<sup>+++</sup> current fraction across the thruster-plume interface.

#### A. Plume Model

MPIC is a hybrid particle-fluid simulation code that computes time-averaged steady state results in three dimensional unstructured computational meshes. Neutral particle dynamics, collisions, and ion particle collisions are simulated using the direct simulation Monte Carlo (DSMC) method. <sup>17</sup> Ion particle dynamics are informed by the particle-in-cell (PIC) method. <sup>18</sup> To avoid the small time steps required to accurately simulate electrons as simulation particles, electrons are modeled as a fluid.

#### 1. DSMC-PIC Model

The plume model uses the electrostatic assumption that allows the electric field to be defined in terms of a scalar electric potential:

$$\mathbf{E} = -\nabla \phi \tag{1}$$

where **E** is the electric field and  $\phi$  is the electric potential. MPIC ignores the effects of magnetic fields so the PIC method moves particles according to the electric component of the Lorentz force:

$$\mathbf{F} = q(\mathbf{E}) \tag{2}$$

where  $\mathbf{F}$  is the force on a particle, and q is the charge of the species. The electric field is calculated at nodal locations on a computational grid and is interpolated to particle positions when updating their velocities.

Collisions are performed stochastically. The No-Time-Counter scheme<sup>17</sup> is used to calculate the total number of potential collision pairs:



$$N_{pairs} = \frac{1}{2} N_P n(\sigma g)_{max} \Delta t \tag{3}$$

where  $N_P$  is the number of macroparticles, n is the number density,  $\Delta t$  is the timestep, and  $(\sigma g)_{max}$  is an estimate of the maximum value of the product of the collisional cross section and the relative speed of the colliding particles within the computational cell. Whether or not a given pair collides is decided by comparing the collision probability with a random number. The collision probability is calculated as the ratio of  $\sigma g$  to  $(\sigma g)_{max}$ . MPIC utilizes the variable hard-sphere model<sup>19</sup> to obtain momentum exchange (MEX) collision cross sections for collisions between neutral atoms. In this model, the cross section is a function of the relative speed:

$$\sigma_{coll} = \sigma_{ref} \left(\frac{g_{ref}}{g}\right)^{2\nu} \tag{4}$$

where the power law exponent,  $\nu$ , is a viscosity fitting parameter. MPIC can also model charge exchange (CEX) collisions. Atom-ion MEX and CEX collision cross sections are modeled using measured data<sup>20</sup> which yields the following semi-empirical formula:

$$\sigma_{CEX}(Kr, Kr^{+}) = 10^{-20} \left( A - B \log_{10}(\epsilon_{coll}) \right) \tag{5}$$

where A and B are fitting parameters and  $\epsilon_{coll}$  is the collision energy in eV. Fitting parameters for krypton single and double charge exchange were empirically derived in Ref. 21. Additionally, MPIC assumes that all charged heavy species are neutralized by any wall interactions.

#### 2. Fluid Electron Model

The electron model employed in this work is the Boltzmann Electron Model. This model begins with the electron momentum equation. The steady electron momentum equation, neglecting the advection term and magnetic field effects, is:

$$0 = -n_e e \mathbf{E} - \nabla p_e + m_e n_e (\mathbf{v_i} - \mathbf{v_e}) \nu_{ei} \tag{6}$$

where e is the elementary charge,  $p_e$  is the electron pressure,  $m_e$  is the electron mass,  $\mathbf{v_i}$  is the ion velocity,  $\mathbf{v_e}$  is the electron velocity, and  $\nu_{ei}$  is the electron-ion collision rate. The Boltzmann relation is obtained by making the following assumptions: the electrons respond instantaneously to any disturbance, the electron fluid is isothermal and collisionless, and the electron pressure obeys the ideal gas law. The result is:

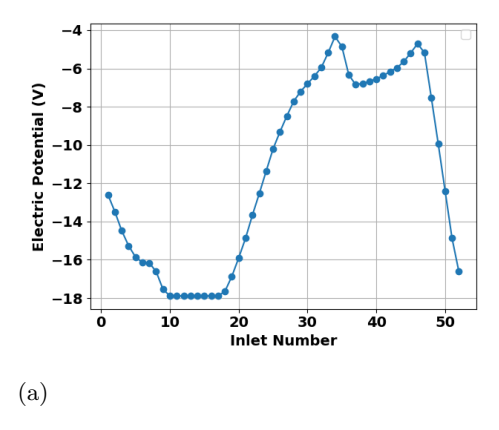
$$\phi = \phi_{ref} + \frac{k_B T_e}{e} ln \left( \frac{n_e}{n_{ref}} \right) \tag{7}$$

where  $\phi_{\rm ref}$  is a reference potential,  $n_e$  is the electron number density,  $n_{\rm ref}$  is a reference electron number density,  $k_B$  is Boltzmann's constant, and  $T_e$  is the constant electron temperature. The additional assumption of quasineutrality in each computational cell allows the electron number density in Eqn. 6 for  $\phi$  to be replaced with the total ion number density which is tracked by MPIC's kinetic models. Plots of the electric potential and electron temperature profiles across the entire thruster-plume interface are shown in Fig. 7. However, the reference potential, reference number density, and electron temperature are set to the potential condition, electron number density, and electron temperature predicted by Hall2De at the centerline near-field coupling interface between Hall2De and MPIC - inlet number fifty-two. The reference conditions are shown in Table.

Table 2: Simulation Boltzmann Electron Model Reference Conditions.

Number Density, $m^{-3}$	Potential, $V$	Temperature, $eV$
$1.603 \times 10^{17}$	-16.6	2.51





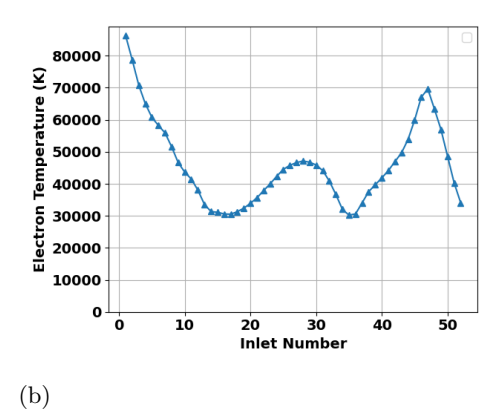


Figure 7: Profiles of (a) electric potential, and (b) electron temperature across the thruster-plume interface.

## B. Facility Pressure Model

MPIC accounts for the background neutral population present in ground-based vacuum chamber tests by using an accurate three dimensional facility geometry represented in the computational mesh and sticking coefficients assigned to facility pump surfaces. The sticking coefficient is a boundary condition assigned to each computational surface; it determines the fraction of particle interactions with that surface that result in the particle sticking to the surface, and therefore being removed from the simulation domain. Previous work has been done to infer sticking coefficients for the PHPK-TM1200i re-entrant vacuum pumps in the University of Michigan's Alec D. Gallimore Large Vacuum Test Facility (LVTF) with the H9 HET operating on xenon.<sup>22</sup> The same sticking coefficient inferred in Ref. 22, 0.26, is assumed to be the nominal sticking coefficient for the pumps in VTF-2 because the cryopumps in VTF-2 are the same model PHPK-TM1200i re-entrant vacuum pumps.

#### C. Sputtering Model

Surface sputter yields are calculated using an equation based on the Eckstein model.<sup>23</sup> The calculated sputter yield is compared against a random number to determine how many sputtered particles will be generated for each individual particle-sputtering surface interaction. The sputter yield equation is calculated as follows:

$$Y(E_i, \theta) = QS_n \frac{\left(\frac{E_i}{E_{Th}} - 1\right)^{\mu}}{\frac{\lambda}{w} + \left(\frac{E_i}{E_{Th}} - 1\right)^{\mu}} \left(\cos\left(\theta_i^c\right)\right)^{-f} exp\left(b\left(1 - \left(\cos\left(\theta_i^c\right)\right)^{-1}\right)\right)$$
(8)

where Y is the total sputter yield,  $E_i$  is the energy of the incident particle in eV, and  $\theta_i$  is the polar angle with respect to the surface of the incident particle in degrees.  $Q, \lambda, \mu, E_{th}, f, c$ , and b are fitting parameters; an example fit for xenon sputtering of carbon is provided in the supplementary material of Ref. 16.  $S_n$ , the nuclear stopping, is calculated as follows:

$$S_n = \frac{0.5 \ln(1 + 1.2288\epsilon)}{\epsilon + 0.1728\sqrt{\epsilon} + 0.008\epsilon^{0.1504}}$$
(9)

where the reduced energy,  $\epsilon$ , is:

$$\epsilon = \frac{a_L}{Z_i Z_s} \frac{4\pi\epsilon_0}{e_{vc}^2} \frac{M_s}{M_i + M_s} E_i \tag{10}$$

where  $\epsilon_0$  is the vacuum permittivity constant in  $C^2eV^{-1}$  Å<sup>-1</sup>,  $e_{vc}$  is the electron charge in C,  $M_i$  and  $M_s$  are the molar mass in g/mol of the incident and sputtered material respectively,  $Z_i$  and  $Z_s$  are the atomic number of the incident and sputtered material respectively, and the Lindhard screening length,  $a_L$ , is calculated as follows:



$$a_L = \left(\frac{9\pi^2}{128}\right)^{\frac{1}{3}} a_0 \left(Z_i^{\frac{2}{3}} + Z_s^{\frac{2}{3}}\right)^{-\frac{1}{2}} \tag{11}$$

where  $a_0$  is the Bohr radius in Å.

Sputter angle is sampled from two coupled distributions for the polar and azimuthal angles with respect to the sputtering surface. The polar angle distribution is a linear combination of two Gaussians:

$$f(\theta_s) = \frac{A}{\sigma_1 \sqrt{2\pi}} e^{-\frac{1}{2} \left(\frac{\theta_s - \mu_1}{\sigma_1}\right)^2} + \frac{1 - A}{\sigma_2 \sqrt{2\pi}} e^{-\frac{1}{2} \left(\frac{\theta_s - \mu_2}{\sigma_2}\right)^2}$$
(12)

where  $\theta_s$  is the polar angle of the sputtered particle in degrees, A is the relative contribution of the forward (j=1) and backward (j=2) sputterants,  $\mu_j$  is the peak sputtered angle, and  $\sigma_j$  is the spread due to inelastic collisions. In MPIC these fitting parameters are bi-linearly interpolated between the incident particle angle and energy from the steady-state tables provided in the supplementary material of Ref. 16. The tables are fit using the Markov Chain Monte Carlo with Delay Rejection Adaptive Method. The azimuthal angle is sampled from a quasi uniform distribution based on the sampled polar angle. If the polar angle is between 0 and 90 degrees then the azimuthal angle is uniformly sampled between -90 and 90 degrees, and if the polar angle is between 0 and -90 degrees then the azimuthal angle is uniformly sampled between 90 and 270 degrees. This quasi-uniform distribution is used to translate the two dimensional angular distribution from Ref. 16 into a full three dimensional angular model in MPIC.

The energy of the sputtered particle is sampled from a log normal function form:

$$g(E_s) = \frac{1}{E_s \sigma_s \sqrt{2\pi}} e^{-\frac{1}{2} \left(\frac{\ln(E_s) - \mu_s}{\sigma_s}\right)^2}$$

$$\tag{13}$$

where  $E_s$  is the energy of the sputtered particle, and  $\mu_s$  and  $\sigma_s$  are fitting parameters. In MPIC these fitting parameters are bi-linearly interpolated between the incident particle angle and energy from the tables provided in the supplementary material of Ref. 16. These fitting parameter tables are populated by an algorithm using maximum likelihood estimation.

Together, the polar angle, azimuthal angle, and energy sampled for each sputtered particle specify the initial velocity vector for each particle. The sputtered particle is born in the simulation at the location where the incident particle impacted the surface, and the once incident particle is then diffusely reflected from the surface at the specified surface temperature.

Sputter particles are transported through the simulation domain using the DSMC method as appropriate. Ref. 16 offers angle and energy-dependent sticking coefficients for carbon-carbon interactions. Because this sticking coefficient is often close to unity and for simplicity, sputtered particles in MPIC are automatically assigned a sticking coefficient of 1.0; this means that all particles born from a sputter interaction (not including the diffusely reflected once incident particle) will stick to any surface they are subsequently incident on regardless of any other wall assigned sticking coefficient.

To increase sputter particle resolution relative to plume and background particle resolutions, MPIC has the capability to scale the particle weight of sputtered particles relative to the particle weight of all other particles. Several sputtered particles are uniquely sampled from the appropriate distributions for each sputtering event until the relative weighting is satisfied. For example, if the simulation particle weight is  $(10)^{12}$ , the relative sputter particle weighting is 10 and a sputtering interaction occurs, MPIC will generate and uniquely sample 10 sputter particles with a particle weight of  $(10)^{11}$ . Due to this variable particle weighting scheme VHS collisions for sputtered carbon particles have not yet been implemented. However, the minimum mean free path of carbon-13 in the simulations is calculated to be on the order ten meters, and the length scale of interest, the distance between sputter source and sputter target, is only about ten centimeters. Therefore, ignoring collisions for carbon-13 will not greatly impact results. Moreover, all of the fitting parameters for the sputter yield, sputter angle, and sputter energy equations from Ref. 16 are for xenon-carbon interactions. The experiments and simulations presented in this paper use krypton as a propellant. However, the xenon-carbon fitting parameters are used under the approximation that the mass ratio of the incident particle to sputtered particle dominates the sputtering interaction and both xenon and krypton are significantly heavier than carbon.



## D. Sensitivity Analysis

To quantify the sensitivity of the sputter deposition results to key aspects of the plume model, a formal sensitivity analysis is performed. Select input variables to MPIC are varied across a conservative yet realistic parameter space and several high fidelity simulations run in order to inform a surrogate model mapping the varied parameters to the quantity of interest: sputter particle deposition rate on the specified collection arrays. A summary of the varied parameters and the domain over which they are varied is provided in Table 3. Typical bounds for sticking coefficient are reported in Ref. 24. Experimental current density measurements taken of similar class HETs from Refs. 25,26 are used to inform bounds for beam current fraction and beam divergence half angle. Nominal ion and electron temperatures are taken from Hall2De simulation and both are bounded from half of nominal to double the nominal based on previous modeling efforts.<sup>27</sup>

For simplicity in generating simulation inputs for several varied parameters, a simplified zero-dimensional HET model is used. In this model neutral krypton is assumed to exit the thruster at the speed of sound with a temperature of 773 K. The ratio of double and triple charged ions is set by the nominal Hall2De simulation. All ions are assumed to accelerate through the full 600 V discharge potential. The ion current, divergence angle, and single charged ion temperature are assigned from the varied beam current, divergence angle, and ion temperature parameters respectively. Using the previously mentioned parameters and the experimentally reported mass flow rate, species number densities and velocities at the thruster exit are determined by conservation of mass and charge. This approach guarantees that the flow properties are consistent with experimental measurements while avoiding the need for expensive, high-fidelity thruster simulations or geometries of complicated coupling schemes.

The varied parameter space is populated using Latin Hypercube Sampling (LHS). MPIC high fidelity simulations are fit to a surrogate model using a Bayesian Optimization of a Gaussian Process Regression (GPR) following Ref. 29. A similar approach, with limited high fidelity samples, was effective in a computational fluid dynamics context. Individual parameter sensitivities are calculated via variance based Sobol' indices  $^{31,32}$  by executing many evaluations of the surrogate model. The surrogate model is evaluated using Monte Carlo samples and the number of surrogate model evaluations is determined such that the residual of each first-order, and each total-effect Sobol' index from the previous set of evaluations drops below  $1 \times 10^{-4}$ .

Parameter	Units	Domain
Sticking Coefficient	-	[0.2, 0.6]
Beam Current Fraction	-	[0.65,  0.95]
Beam Divergence Half Angle	Degrees	[20, 35]
Ion Temperature	$\mathrm{eV}$	[4.275, 17.1]
Electron Temperature	$\mathrm{eV}$	[1.25, 5]

Table 3: Summary of varied input parameters to MPIC.

## IV. Results

## A. Sputter Model Verification

To verify that the Eckstein based sputter model is correctly implemented into MPIC, several test cases are designed so that mono-energetic ions impact a sputterable surface at a specified angle. These test cases are full MPIC simulations in very simple geometric domains with hundreds of computational cells (compared to hundreds of thousands of computational cells in vacuum chamber simulations). The simulations output an average sputter yield of the sputterable surface, a polar angle distribution of the sputtered carbon particles as they are born into the simulation, and an energy distribution of carbon particles as they are born into the simulation. Average sputter yield is then compared to an expected yield calculated from Eq. 8, and the angle and energy distributions are compared to expected distributions calculated by Eqs. 12 and 13. Comparisons of simulation sputter yield to expected sputter yield, and the route mean squared (RMS) error of energy and polar angle distributions for three test cases are summarized in Table 4. The simulation polar angle and energy distributions are compared to expected distributions for the three cases: the 500 eV and normal incidence case is shown in Fig. 8, the 750 eV and 45 degree incidence case in Fig. 9, and the 1000



eV and 75 degree incidence case in Fig. 10. Good agreement is found in all three cases for average sputter yield, carbon polar angle distribution, and carbon energy distribution.

Table 4: Comparing expected and simulated sputter yields and particle angle and energy distributions for test cases.

Incident Energy, eV	Incident Angle, Degrees	Sputter Yield Percent Difference	Energy RMS Error, eV	Polar Angle RMS Error, Degrees
500	0	0.086%	$6.28\times10^{-5}$	$1.02\times10^{-4}$
750	45	0.094%	$1.97\times 10^{-4}$	$6.62\times10^{-5}$
1000	75	0.019%	$5.49\times10^{-4}$	$3.41\times10^{-5}$

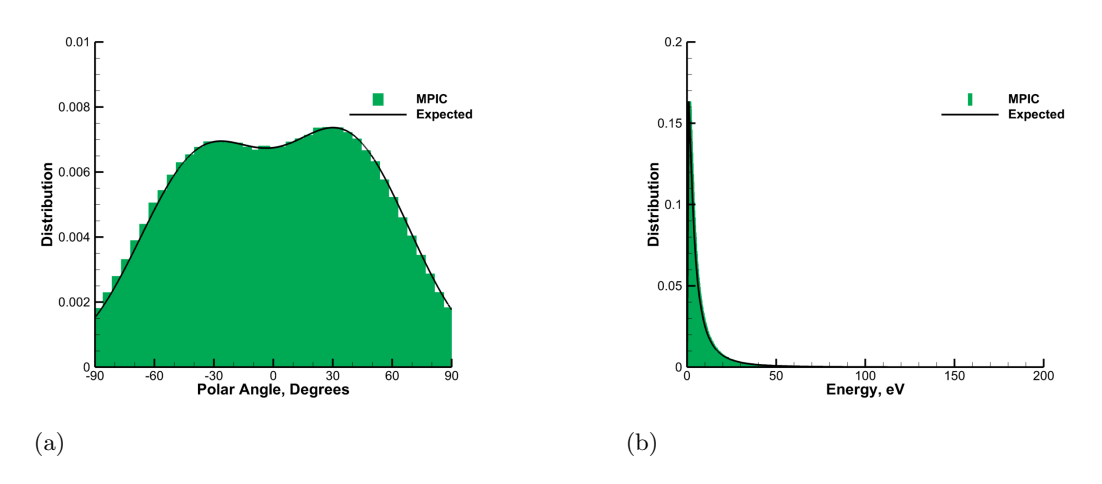


Figure 8: Comparisons of (a) simulated carbon polar angle distribution to expected distribution and (b) simulated carbon energy distribution to expected distribution for 500 eV normal incident xenon.

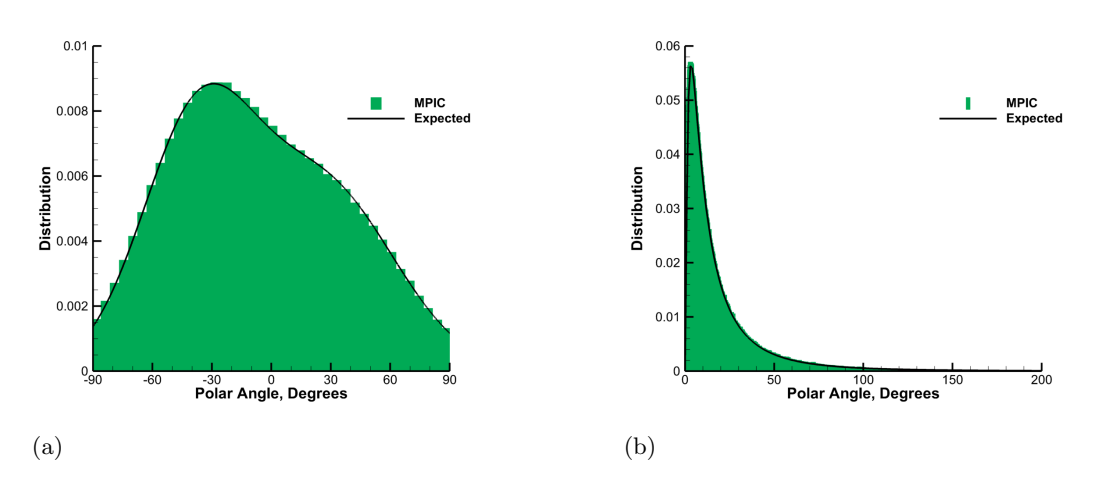


Figure 9: Comparisons of (a) simulated carbon polar angle distribution to expected distribution and (b) simulated carbon energy distribution to expected distribution for 750 eV 45 degree incident xenon.



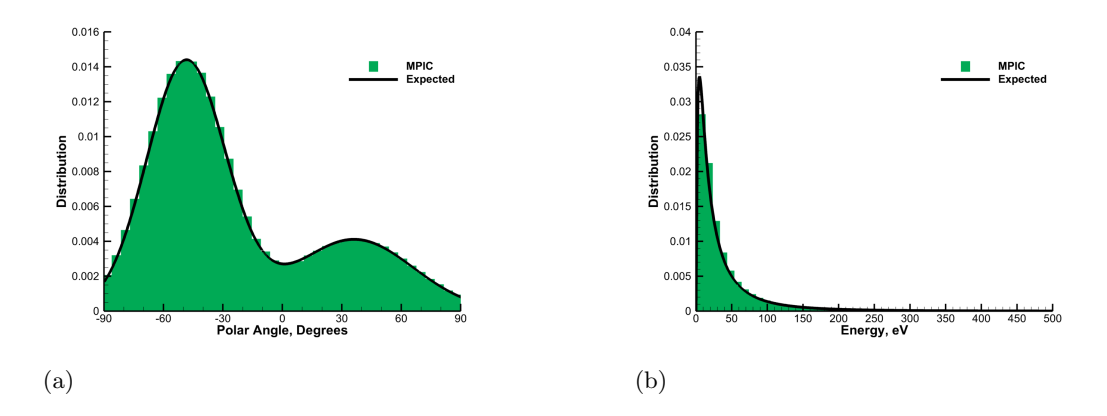


Figure 10: Comparisons of (a) simulated carbon polar angle distribution to expected distribution and (b) simulated carbon energy distribution to expected distribution for 1000 eV 75 degree incident xenon.

## B. Sputtering Simulations

High fidelity vacuum chamber simulations of VTF-2 with a physically accurate model of the sputtering experimental set-up described above are run in MPIC. Graphics of the computational mesh used to represent the sputtering experiments are shown in Fig. 11. The mesh cells of the collection arrays are specifically designed so that one square cell corresponds to one of the sixteen collection array substrates from the experiment; therefore the deposition rate on each computational cell can be individually sampled and compared to the experiment. Krypton particles are run to steady state over three seconds of physical time, then the sputtering model is turned on and the carbon deposition rate on the collection arrays reaches steady state after an additional one and a half seconds of physical time. Simulation statistics are then sampled every iteration for an additional 150,000 iterations. A comparison between the simulated and experimental current density traces is shown in Fig. 12. The simulation current density over-predicts the experimental current density over the first ten degrees from the centerline, then under-predicts until about thirty degrees, and has good agreement at high angles. Contour plots of singly charged krypton number density and axial velocity are shown in Fig. 13. The effect of the sputtering experiment, in particular the heat shield, can be seen by significant decreases in both number density and velocity plots around five thruster diameters downstream from the thruster exit. Plots of the distribution of incident angles and energies of all particles that cause a sputter event are shown in Fig. 14. The most probable incident angle is about seven degrees whereas the most probable energy is around 570 eV. The high angle tail of the polar angle distribution is due to particles glancing against the side of the cylindrical carbon-13 target.

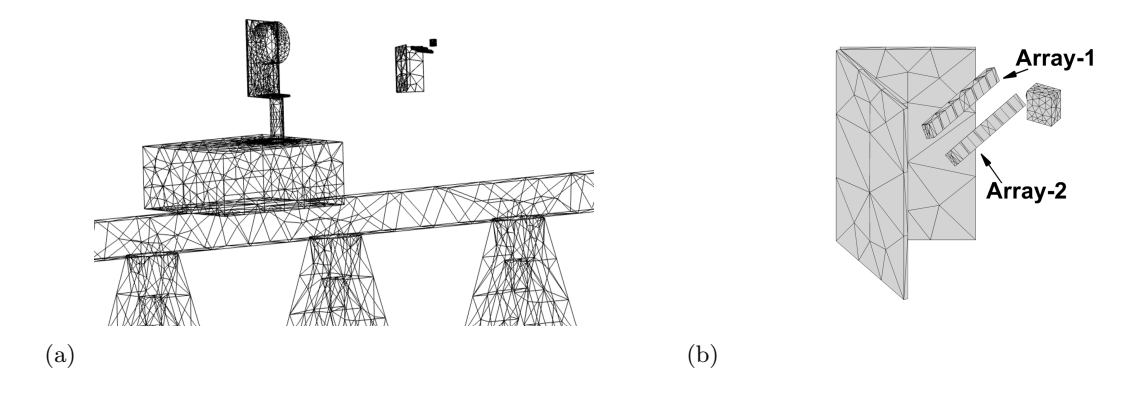


Figure 11: (a) Computational mesh of thruster, thrust stand, floor supports, and sputtering experimental set-up in VTF-2 with chamber walls removed for clarity. (b) Zoomed in view of sputtering experiment mesh heat shield, collection arrays, and carbon-13 target.



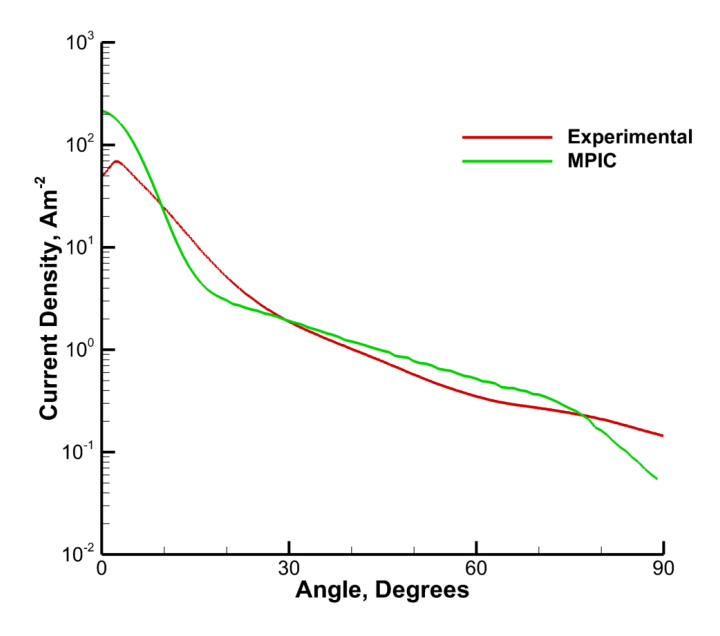


Figure 12: Comparison of simulation and experimental current density trace 1.0 m from the thruster exit.

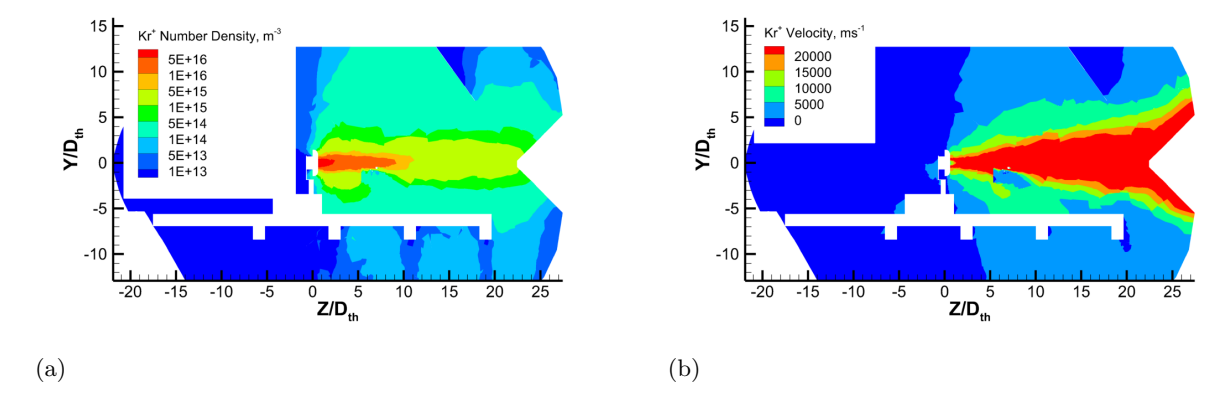


Figure 13: 2D slices of 3D solutions of Kr<sup>+</sup> (a) number density contours, and (b) axial velocity contours.

The most probable incident angle and energy from the incident distributions in Fig. 14 are used in Eqs. 12 and 13 to determine expected distributions of the carbon angle and energy born from the carbon-13 target. These expected distributions are plotted against the simulated distributions from MPIC in Fig. 15. The two Gaussian peaks of the simulation angular distribution are more even than the most probable incident angle predicts; this could be due to the high angle tail of incident particles. The most probable incident energy predicts the carbon sputter energy very closely. Figure 16 shows a comparison of MPIC's predicted deposition rate of sputtered carbon-13 and the experimental measurement. There is very good agreement between simulation and experiment for Array-2, the closer array, but about a factor of two over-prediction of the deposition rate on Array-1. The simulation results have an additional dependence on polar angle (arrays one and two are at different polar angles relative to the carbon source) whereas the experimental data appear to vary primarily with radial distance from the target.



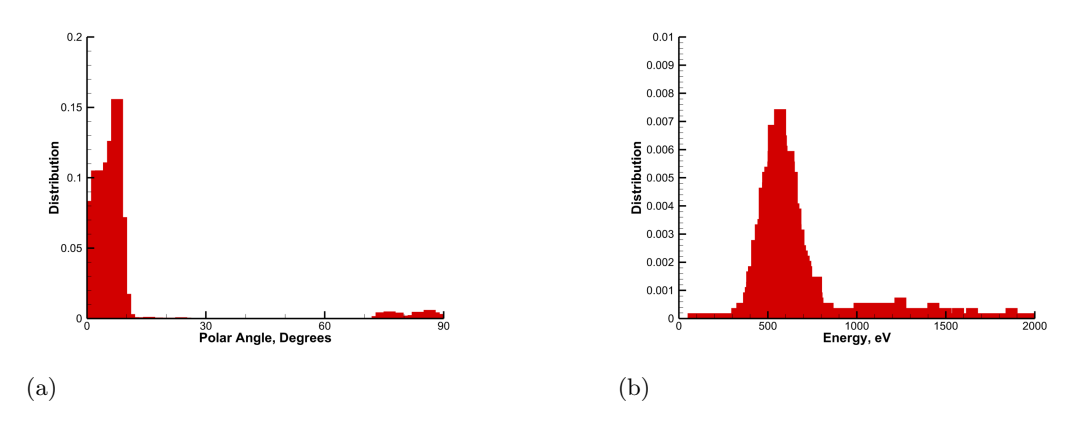


Figure 14: Distributions of (a) incident polar angle and (b) energy of all particles that cause sputter event on the carbon-13 target.

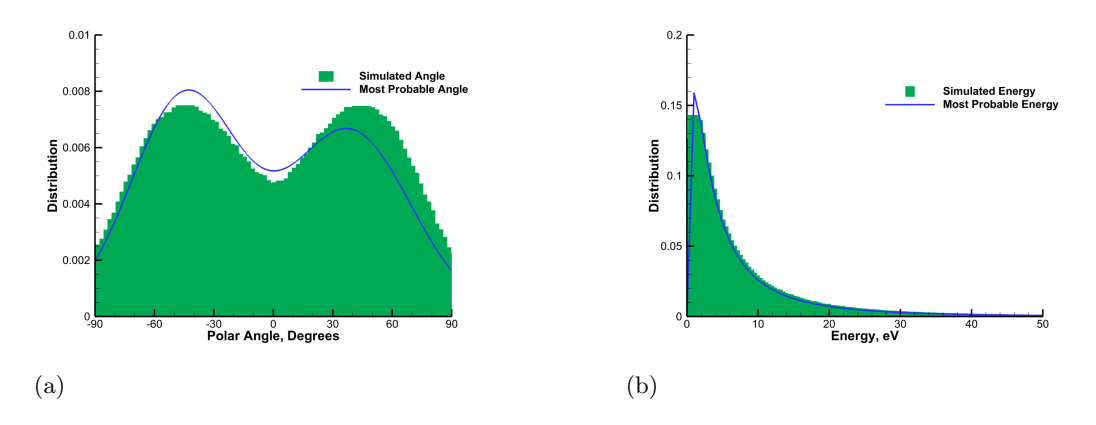


Figure 15: Distributions of sputtered carbon particle (a) polar angle and (b) energy compared to expected distributions based on most probable incident angle and energy.

An additional simulation is run with the graphite beam dump in VTF-2 allowed to sputter carbon-12 to approximate facility-wide sputtering. In this simulation the flux of carbon-12 is measured through an area fifteen centimeters directly downstream of the thruster face. This flux is used as a means to determine when the sputtered particles have reached steady state, and to provide a predicted carbon flux into the thruster. The measured region is downstream of the thruster exit plane because the interface between the thruster code and plume code extends into the near field plume, so the domain of the plume code only extends about fifteen centimeters from the thruster face. The steady state mass flux of carbon-12 to this region is simulated to be  $4.768 \times 10^{-9} \text{ kg/m}^2 \text{ s}$ . Figure 17 shows number density contours in a two-dimensional slice of the three dimensional solution of carbon-13 near the thruster and sputtering experimental set-up, and carbon-12 throughout the whole facility.

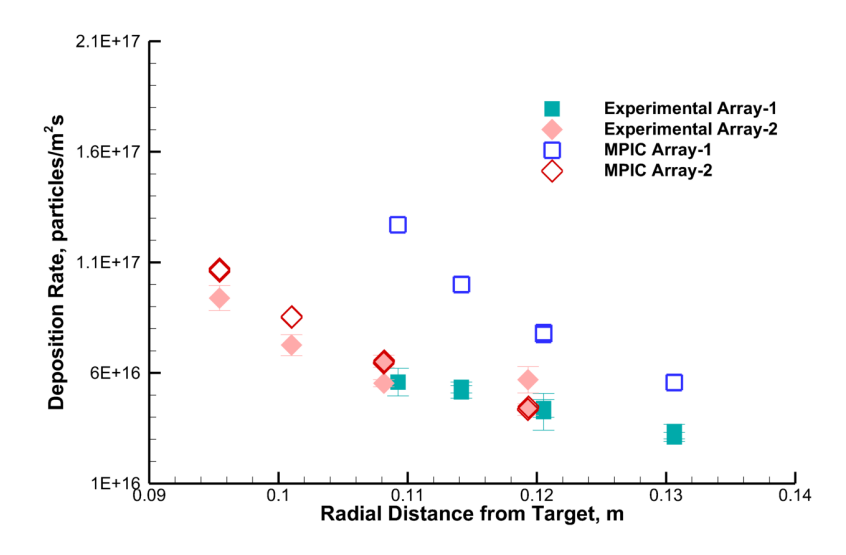


Figure 16: Comparison of predicted and experimentally measured sputtered carbon-13 deposition rate onto each collection substrate.

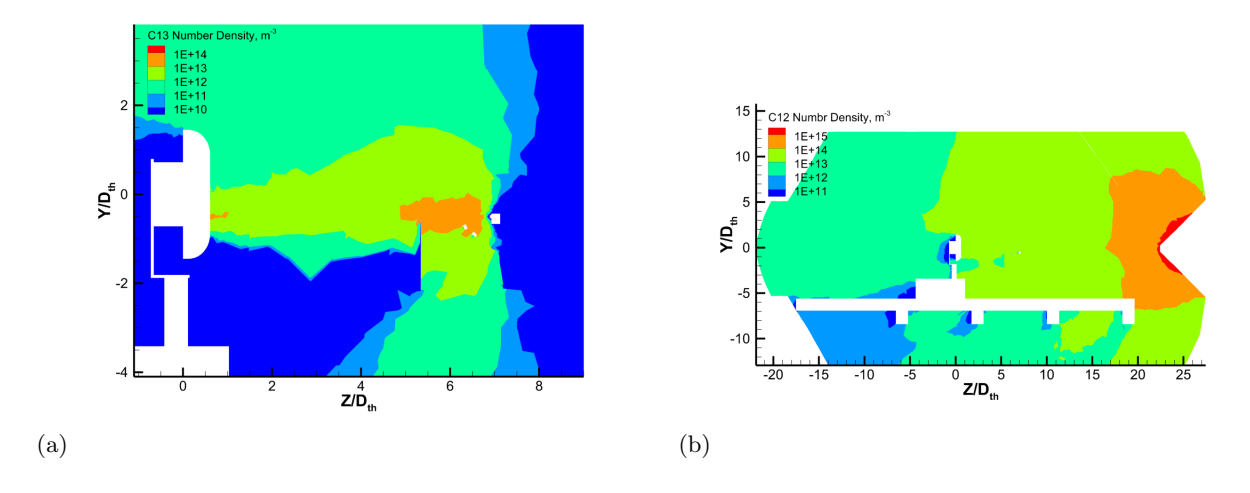


Figure 17: Number density contours in 2D slices of 3D solutions of (a) carbon-13 near thruster and sputtering experimental set-up, and (b) of carbon-12 throughout VTF-2.

## C. Sensitivity Analysis

Fifty high fidelity MPIC simulations are run across an LHS parameter space. Figure 18 shows the span of current densities and collection array deposition rates represented by the fifty high fidelity runs. Pressure contours near the thruster and sputtering experiment for the minimum and maximum pressure cases of the fifty runs are shown in Fig. 19. The five varied parameters summarized in Table 3 are then used to train a Bayesian optimized GPR on the response of average collection array carbon-13 deposition rate. The GPR has a cross-validated coefficient of determination,  $R^2$ , of 0.98 indicating strong agreement between surrogate model predictions and high fidelity simulation results. A plot of the surrogate validation response and the high fidelity response against ion temperature is shown in Fig. 20. To perform the Sobol' variance based sensitivity analysis, the GPR is evaluated  $2^{27}$ , unique times. With this surrogate data set, the calculated Sobol' indices residual falls below  $1 \times 10^{-4}$  and the resulting first-order and total-effect Sobol' indices are plotted in Fig. 21.



The total-effect Sobol' indices are approximately equal to the first-order Sobol' indices indicating that the variance in target deposition rate is dominated by the direct effects of individual parameters rather than interaction effects of the parameters. The Sobol' index for sticking coefficient is virtually zero indicating that the pump sticking coefficient in the vacuum chamber has very little effect on the quantity of interest, sputtered particle deposition rate on the collection arrays. Electron temperature has a Sobol' index of about 0.06. Therefore, uncertainty in the electron temperature does not contribute very much uncertainty in the final quantity of interest, and using the Boltzmann electron model which assumes isothermal electrons is not a large detriment. The beam current fraction and beam divergence half angle have Sobol' indices of 0.15 and 0.21, respectively, suggesting that they each have a moderate effect on carbon deposition rate. Therefore, having an accurate simulated current density trace is an important step in ensuring accurate sputtering simulation. Above all other varied parameters, however, variances in ion temperature tend to create the largest variances in carbon deposition rate with ion temperature having a Sobol' index of about 0.57. It is thus critical to compare ion energy distribution functions between simulation and experiment to ensure accurate simulation ion temperatures.

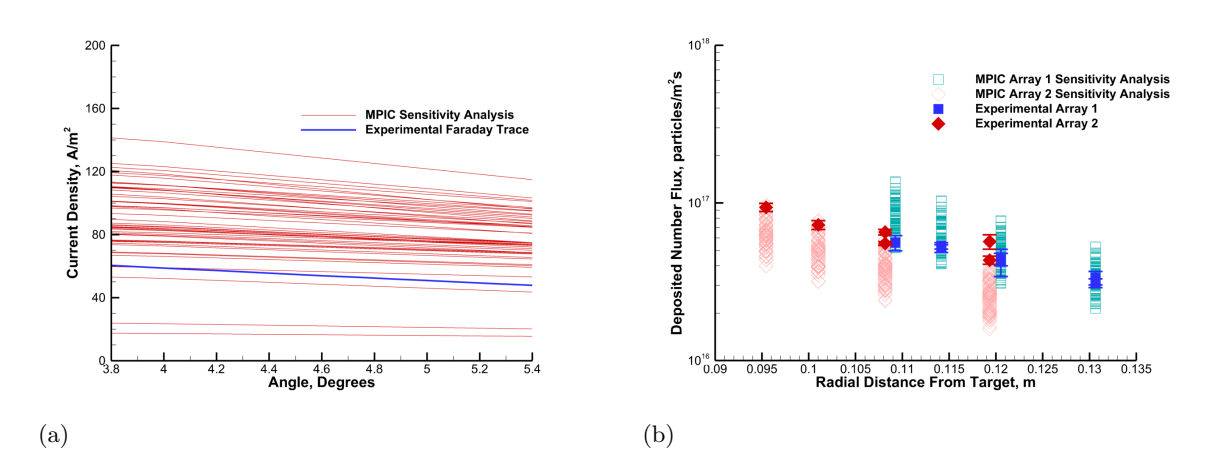


Figure 18: (a) Current density traces for all 50 high fidelity simulations in sensitivity analysis compared to experimental current density trace across range of angles of sputtering experimental set-up. (b) Sputtered carbon-13 deposition rate onto each collection substrate for all 50 high fidelity simulations in sensitivity analysis compared to experimental measurement.

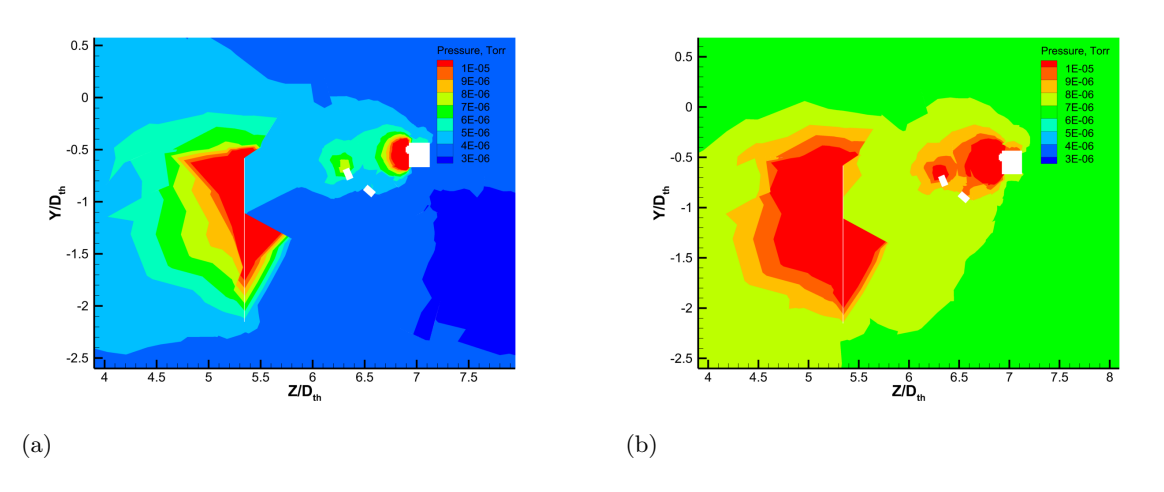


Figure 19: Pressure (torr) contours in 2D slices of 3D solutions near sputtering experimental set-up of sensitivity analysis for (a) minimum pressure case and (b) maximum pressure case.



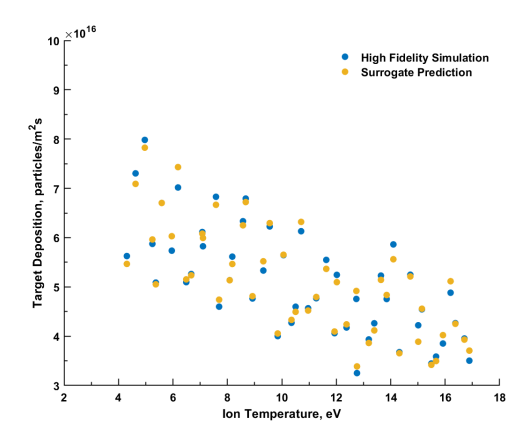


Figure 20: Surrogate model response of target deposition rate compared to high fidelity prediction of target deposition rate as a function of assumed thruster exit ion temperature.

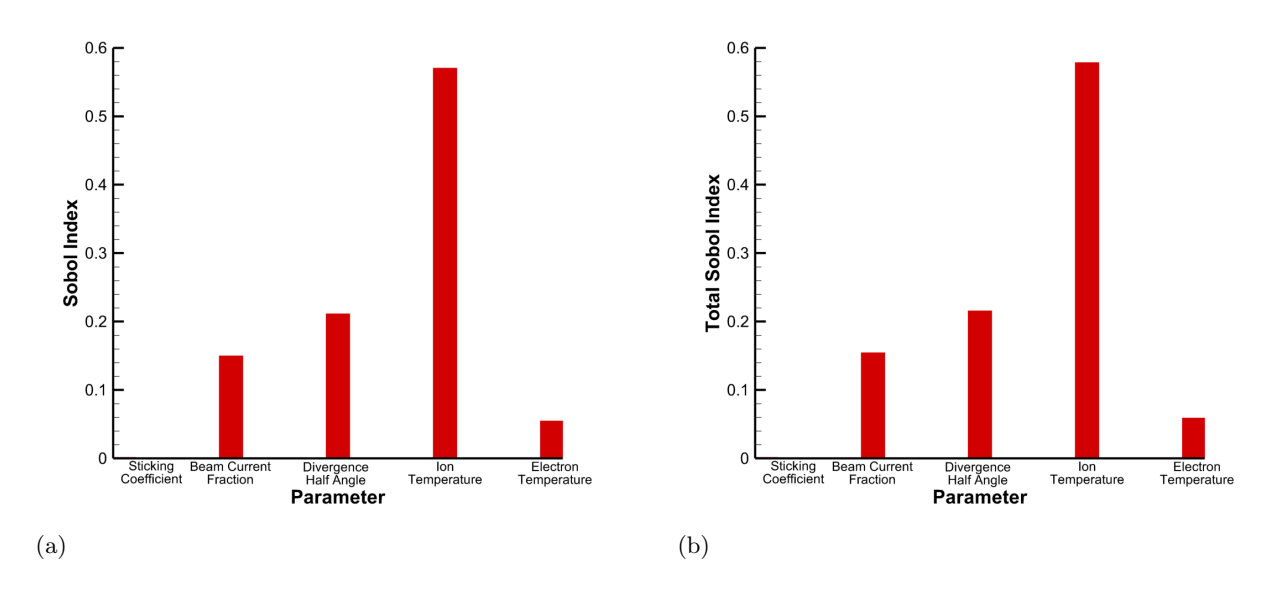


Figure 21: (a) First-order Sobol' indices from sensitivity analysis. (b) Total-effect Sobol' indices from sensitivity analysis.

## V. Conclusions and Future Work

A reduced order sputter model was implemented into the three dimensional hybrid particle-fluid plume simulation code MPIC. The sputter model predicts surface sputter yields, sputtered particle angles, and sputtered particle energies. The particle methods in MPIC then transport sputtered material throughout the computational domain. The reduced order sputter yields, and sputter angle and energy profiles were verified to be producing expected results within MPIC simulations. Simulations were then run to mimic an experimental set-up that tracked isotopically unique carbon sputtering from a specific sputter source to specific collection arrays. Comparisons between simulated carbon deposition rate on the collection arrays and experimental results showed good agreement on one of the collection arrays and a factor of two disagreement on the other. This inconsistency indicates that there may be missing physics in the plume model and/or the sputtering model. To elucidate the importance of plume model accuracy in the prediction of sputter tracking, a sensitivity analysis was performed in which fifty high fidelity simulation results were used to inform a GPR surrogate model. That surrogate model was then evaluated using a Monte Carlo method to



gauge the sensitivity of carbon deposition rate on the collection arrays to simulation sticking coefficient, beam current, beam divergence angle, ion temperature, and electron temperature. The variance in deposition rate was mostly explained by variance in the ion temperature. Beam current and beam divergence angle variances had a modest effect on the deposition rate, and electron temperature and sticking coefficient had very little effect. Going forward, any sputtering comparisons between simulations and experiments should also compare simulated ion energy distribution functions to experimental distributions collected from a retarding potential analyzer.

Although one could surmise that one or perhaps several of the simulations from the sensitivity analysis perfectly match the experimental deposition rate based on Fig. 18 (b), an investigation into the results of individual simulations showed a global dependence of the predicted carbon-13 deposition rate on the angle from carbon source to destination. Many of the sensitivity analysis simulations do predict the average carbon-13 deposition rate better than the nominal case. In fact, seventeen of the simulations have less than a 10% difference in sputter deposition rate averaged over both collection arrays, compared to 54% in the nominal case. However, inspection of these cases consistently shows over-prediction for Array-1 balanced out by under-prediction for Array-2. Both the nominal case predicting average deposition rate worse than many sensitivity analysis cases, and the inconsistent trend with angle from target to destination for simulation and experiment highlight the need for accurate plume characterization and an improved sputter model.

Future work will explore implementing alternate sputtering models and using experimental sputter fits. Despite the insensitivity of sputtered particle deposition rate to electron temperature, the effect of an electron model that does not assume isothermal or collisionless electrons will also be explored with the goal of improving the agreement between simulation and experimental current density measurements. If these additions to the modeling improve agreement between simulations and experiments, further extrapolations of facility wide sputtering and in-space sputtering should also be more accurate.

## Acknowledgments

This work was supported by NASA through the Joint Advanced Propulsion Institute, a NASA Space Technology Research Institute, grant number 80NSSC21K1118. This work utilized resources from the University of Colorado Boulder Research Computing Group, which is supported by the National Science Foundation, the University of Colorado Boulder, and Colorado State University. Resources supporting this work were also provided by the NASA High-End Computing Program through the NASA Advanced Supercomputing Division at Ames Research Center.

## References

<sup>1</sup>Saleh, J. H., Geng, F., Ku, M., and Walker II, M. L., "Electric propulsion reliability: Statistical analysis of on-orbit anomalies and comparative analysis of electric versus chemical propulsion failure rates," *Acta Astronautica*, Vol. 139, 2017, pp. 141–156.

<sup>2</sup>Goebel, D. M. and Katz, I., Fundamentals of Electric Propulsion: Ion and Hall Thrusters, JPL Space Science and Technology Series, John Wiley and Sons, New Jersey, 2008.

<sup>3</sup>Levchenko, I., Goebel, D. M., and Bazaka, K., "Electric propulsion of spacecraft," *Physics Today*, Vol. 75, No. 9, 2022, pp. 38–44

<sup>4</sup>Randolph, T., Kim, V., Kaufman, H., Kozubsky, K., Zhurin, V., and Day, M., "Facility effects on stationary plasma thruster testing," 23rd International Electric Propulsion Conference, No. 844, The Electric Rocket Propulsion Society Worthington, OH, 1993, pp. 13–16.

<sup>5</sup>Gilland, J. H., Williams, G., Burt, J. M., and Yim, J., "Carbon back sputter modeling for hall thruster testing," 52nd AIAA/SAE/ASEE Joint Propulsion Conference, 2016, p. 4941.

<sup>6</sup>Oh, D. Y., Hastings, D. E., Marrese, C. M., Haas, J. M., and Gallimore, A. D., "Modeling of stationary plasma thruster-100 thruster plumes and implications for satellite design," *Journal of Propulsion and Power*, Vol. 15, No. 2, 1999, pp. 345–357.

<sup>7</sup>Nishii, K., Clark, S., Tran, H., Levin, D. A., Rovey, J., and Chew, H. B., "Carbon Sputtering and Transportation in a Ground Facility during Electric Propulsion Testing," *AIAA AVIATION 2022 Forum*, 2022, p. 3497.

<sup>8</sup>Qi, J., Wu, X., Yi, T., Ren, J., Wang, Y., Zhang, Z., Zhang, G., Wang, W., and Tang, H., "The Sputtering-Deposition Balance in the Beam and backflow Regions of Electric propulsion plume," *Acta Astronautica*, 2025.

<sup>9</sup>Thomas, A., Lemmer, K., Cabrera, J., Walker, M. L. R., and Topham, T. e. a., "High-Speed Far-Field Energy Measurements in a 9-kW Hall Effect Thruster for Model Inference and Calibration," 38th International Electric Propulsion Conference, 2024.

<sup>10</sup>Clark, S., Thompson, R., and Rovey, J. L., "Spatially Resolved Measurements of 13C Transport in Electric Propulsion Testing," 38th International Electric Propulsion Conference, 2024.



- <sup>11</sup>Hofer, R. R., Cusson, S. E., Lobbia, R. B., and Gallimore, A. D., "The H9 magnetically shielded Hall thruster," 35th International Electric Propulsion Conference, Electric Rocket Propulsion Society, 2017, pp. 2017–232.
- <sup>12</sup>Lipscomb, C. P., Simulation of Hall Thruster Plasma Plume Expansion in Vacuum Chamber and Space Environments, Ph.D. thesis, University of Colorado Boulder, 2025, Ph.D. Dissertation, forthcoming.
- <sup>13</sup>Mikellides, I. G. and Katz, I., "Numerical simulations of Hall-effect plasma accelerators on a magnetic-field-aligned mesh," *Physical Review E—Statistical, Nonlinear, and Soft Matter Physics*, Vol. 86, No. 4, 2012, pp. 046703.
- <sup>14</sup>Lopez Ortega, A. and Mikellides, I. G., "The importance of the cathode plume and its interactions with the ion beam in numerical simulations of Hall thrusters," *Physics of Plasmas*, Vol. 23, No. 4, 2016.
- <sup>15</sup>Lipscomb, C. P., Stasiukevicius, M. J., Boyd, I. D., Hansson, K. B., Marks, T. A., Brick, D. G., and Jorns, B. A., "Evaluation of H9 Hall Thruster Plume Simulations using Coupled Thruster and Facility Models," 38th International Electric Propulsion Conference, 2024.
- <sup>16</sup>Tran, H. and Chew, H., "Surface morphology and carbon structure effects on sputtering: Bridging scales between molecular dynamics simulations and experiments," *Carbon*, Vol. 205, 2023, pp. 180–193.
  - <sup>17</sup>Bird, G. A., Molecular gas dynamics and the direct simulation of gas flows, Oxford university press, 1994.
  - <sup>18</sup>Birdsall, C. K. and Langdon, A. B., Plasma physics via computer simulation, CRC press, 2018.
- <sup>19</sup>Bird, G. A., "Monte-Carlo simulation in an engineering context," Progress in Astronautics and Aeronautics, Vol. 74, 1981, pp. 239–255.
- <sup>20</sup>Miller, J. S., Pullins, S. H., Levandier, D. J., Chiu, Y.-h., and Dressler, R. A., "Xenon charge exchange cross sections for electrostatic thruster models," *Journal of Applied Physics*, Vol. 91, No. 3, 2002, pp. 984–991.
- <sup>21</sup>Hause, M. L., Prince, B. D., and Bemish, R. J., "Krypton charge exchange cross sections for Hall effect thruster models," Journal of Applied Physics, Vol. 113, No. 16, 2013.
- <sup>22</sup>Lipscomb, C., Boyd, I. D., Hansson, K. B., Eckels, J., and Gorodetsky, A., "Simulation of Vacuum Chamber Pressure Distribution with Surrogate Modeling and Uncertainty Quantification," AIAA SCITECH 2024 Forum, 2024, p. 2369.
- <sup>23</sup>Eckstein, W. and Preuss, R., "New fit formulae for the sputtering yield," *Journal of Nuclear Materials*, Vol. 320, No. 3, 2003, pp. 209–213.
- <sup>24</sup>Walker, M. L., Gallimore, A. D., Boyd, I. D., and Cai, C., "Vacuum chamber pressure maps of a Hall thruster cold-flow expansion," *Journal of Propulsion and Power*, Vol. 20, No. 6, 2004, pp. 1127–1132.
- <sup>25</sup>Reid, B. M. and Gallimore, A. D., "Near-field ion current density measurements of a 6-kW Hall thruster," 31st International Electric Propulsion Conference, Vol. 124, 2009.
- <sup>26</sup>Jovel, D. R., Cabrera, J. D., and Walker, M. L., "Current pathways model for hall thruster plumes in ground-based vacuum test facilities: measurements and observations," *Journal of Electric Propulsion*, Vol. 3, No. 1, 2024, pp. 35.
- <sup>27</sup>Boyd, I. D. and Dressler, R. A., "Far field modeling of the plasma plume of a Hall thruster," *Journal of applied physics*, Vol. 92, No. 4, 2002, pp. 1764–1774.
- <sup>28</sup>Helton, J. C. and Davis, F. J., "Latin hypercube sampling and the propagation of uncertainty in analyses of complex systems," *Reliability Engineering & System Safety*, Vol. 81, No. 1, 2003, pp. 23–69.
- <sup>29</sup>Gelbart, M. A., Snoek, J., and Adams, R. P., "Bayesian optimization with unknown constraints," arXiv preprint arXiv:1403.5607, 2014.
- <sup>30</sup>Morita, Y., Rezaeiravesh, S., Tabatabaei, N., Vinuesa, R., Fukagata, K., and Schlatter, P., "Applying Bayesian optimization with Gaussian process regression to computational fluid dynamics problems," *Journal of Computational Physics*, Vol. 449, 2022, pp. 110788.
- <sup>31</sup>Sobol, I. M., "Global sensitivity indices for nonlinear mathematical models and their Monte Carlo estimates," *Mathematics and computers in simulation*, Vol. 55, No. 1-3, 2001, pp. 271–280.
- <sup>32</sup>Saltelli, A., Ratto, M., Andres, T., Campolongo, F., Cariboni, J., Gatelli, D., Saisana, M., and Tarantola, S., *Global sensitivity analysis: the primer*, John Wiley & Sons, 2008.

